Atmos. Chem. Phys., 26, 11909–11921, 2026
https://doi.org/10.5194/acp-26-11909-2026

Atmospheric Chemistry and Physics
Open Access
EGU

Measurement report: Development of a portable peroxy radical measurement system and application for diagnosing local ozone formation and transport

Rujia Tang[1,2,★], Zelong Zheng[1,2,★], Yiming Wang[1,2], Hongxia Liu[1,2], Xiaorui Chen[1,2], and Haichao Wang[1,2]

[1]School of Atmospheric Sciences, Sun Yat-sen University, Southern Marine Science and Engineering Guangdong Laboratory (Zhuhai), Zhuhai, 519082, China
[2]Guangdong Provincial Observation and Research Station for Climate Environment and Air Quality Change in the Pearl River Estuary, Key Laboratory of Tropical Atmosphere-Ocean System, Ministry of Education, Zhuhai, 519082, China
★These authors contributed equally to this work.

Correspondence: Xiaorui Chen (chenxr95@mail.sysu.edu.cn)

Received: 20 January 2026 – Discussion started: 10 February 2026
Revised: 26 May 2026 – Accepted: 25 June 2026 – Published: 21 August 2026

Abstract. Atmospheric total peroxy radicals RO_2^* ($RO_2^* = HO_2 + \sum RO_2$) play central roles in tropospheric chemistry, governing the formation of ozone and secondary aerosols. However, due to their extremely low concentrations and high reactivity, direct observation of RO_2^* remains challenging. In this study, a compact instrument for in-situ measurement of RO_2^* was developed by combining the Peroxy Radical Chemical Amplification (PERCA) technique with Cavity-Enhanced Absorption Spectroscopy (CEAS). Using a pure HO_2 standard for calibration, the system can achieve a chemical chain length of 30 and an optimal detection limit of 0.38 pptv (1σ, 3 min), enabling highly sensitive measurements of ambient peroxy radicals. The self-constructed PERCA–CEAS system was successfully deployed in a field campaign during autumn in Zhuhai to observe ambient RO_2^*. During the observation period, the mean daytime RO_2^* was 31.11 ± 18.87 pptv, which resulted in an average $P(O_3)$ of 14.41 ± 17.04 ppbv h^{-1}. The comparison of O_3 variation and derived $P(O_3)$ indicates that the daytime ozone enhancement in Zhuhai was primarily driven by local photochemical production, while regional transport acted mainly as an export effect. Our results demonstrate that a compact PERCA–CEAS system is capable of ambient RO_2^* measurements and suggest the need of diagnosing O_3 formation pattern with the constraint of high time-resolution RO_2^* concentration.

1 Introduction

In the troposphere, total peroxy radicals RO_2^* ($RO_2^* = HO_2 + \sum RO_2$) are key reactive species that drive photochemical reaction chains in the atmosphere (Monks, 2005). The production and recycling of RO_2^* determine both the persistence and efficiency of photochemical reactions. The continual regeneration of NO_2 through radical–NO_x chain reactions sustains ozone production and leads to its accumulation (Orlando and Tyndall, 2012; Wang et al., 2022). Moreover, the removal of RO_2^* also contributes to the formation of secondary organic aerosols (Chen et al., 2022; Ehn et al., 2014; Zou et al., 2025), which plays a crucial role in regional air quality and climate impacts (Liang et al., 2024). Therefore, understanding the spatiotemporal variations of RO_2^* is essential for elucidating the evolution of regional atmospheric oxidation capacity and assessing pollution formation potential.

Significant advancements have been made in atmospheric peroxy radical measurement techniques over the past few decades, primarily categorized into two technological path-

ways: direct and indirect measurements (Gao et al., 2023). The microwave-induced electron spin resonance (MIESR) method identifies radicals through the resonance of unpaired electrons, providing the most direct evidence of their detection. However, MIESR suffers from low sensitivity and complex operation requirements (Mihelcic et al., 1985, 1990). Indirect measurement techniques detect RO_2^* by converting it into measurable species through chemical reactions. For example, the laser-induced fluorescence (LIF) technique determines RO_2^* concentrations by measuring the OH fluorescence signal generated from the reaction between RO_2^* and NO. This method offers high sensitivity and selectivity, whereas it requires a complex setup and is prone to environmental interferences (Lu et al., 2012; Whalley et al., 2013). The peroxy radical chemical ionization mass spectrometry (PerCIMS) method converts RO_2^* into characteristic ions through ion–molecule reactions, enabling highly sensitive and selective quantification of specific radicals (Edwards et al., 2003; Hornbrook et al., 2011). Unlike other approaches, the peroxy radical chemical amplification (PERCA) measures RO_2^* by amplifying its signal into a large amount of NO_2 through a chain reaction. The PERCA system has relatively high sensitivity to atmospheric RO_2 radicals. The simple construction and routine maintenance for this system ensure the stable measurement on the field. As a result, PERCA has been widely employed in atmospheric observations (George et al., 2020; Liu and Zhang, 2014; Wei et al., 2023).

In the PERCA system, NO and CO are introduced to drive chain reactions that amplify peroxy radicals into detectable NO_2 signals. When sampled air enters the reactor, RO_2 reacts with NO to produce NO_2 and HO_2 (Reactions R1 and R2). The HO_2 then reacts with excess NO to generate OH and NO_2 (Reaction R3), and the OH reacts with CO to recycle back to HO_2 (Reaction R4). Through this chain reaction cycle, the low-concentration peroxy radical signal is progressively amplified into a high-concentration NO_2 signal (Cantrell et al., 1996). The chemical chain length (CL), defined as the average number of radical propagation cycles occurring within the reactor, serves as a quantitative indicator of the amplification efficiency. The magnitude of CL is governed by the competing rates of radical propagation, termination reactions, and physical losses inside the reactor (Kartal et al., 2010; Reichert et al., 2003). Once the amplified NO_2 concentration (ΔNO_2) is determined, the concentration of RO_2^* in ambient air can be derived using the calibrated CL value according to Eq. (1).

$$RO_2 + NO \rightarrow RO + NO_2 \quad \text{(R1)}$$

$$RO + O_2 \rightarrow HO_2 + RCHO \quad \text{(R2)}$$

$$HO_2 + NO \rightarrow OH + NO_2 \quad \text{(R3)}$$

$$OH + CO\,(+M) \rightarrow HO_2 + CO_2\,(+M) \quad \text{(R4)}$$

$$\left[RO_2^*\right] = \frac{\Delta[NO_2]}{CL} \quad (1)$$

Significant progress has been made in peroxy radical chemistry observations and modeling studies in China in recent years. However, most field measurements have been conducted in the major city clusters, such as North China Plain (Ma et al., 2019; Tan et al., 2017, 2018b), the Yangtze River Delta (Lou et al., 2022; Ma et al., 2022), and the Pearl River Delta (Lu et al., 2012; Tan et al., 2019; Yang et al., 2022), while other regions remain underexplored. In addition, RO_2^* studies have primarily focused on the urban and inland areas, with limited exploration within the coastal boundary layer (Zhang et al., 2024). The lack of peroxy radical measurements would also constrain direct assessment of photochemical ozone production. In-situ measurements of ambient RO_2^* provide a direct basis for calculating local $P(O_3)$, as previous studies have demonstrated that observed peroxy radical concentrations enable quantitative assessment of instantaneous ozone production rates and its related chemistry across diverse chemical environments (Sommariva et al., 2011; Thornton et al., 2002). Furthermore, the calculated local $P(O_3)$ combined with the observed O_3 variation provides a powerful means to quantify the contribution of ozone transport (Tan et al., 2021). Therefore, developing portable and high-time-resolution RO_2^* measurement techniques and applying them to diverse atmospheric environments are crucial for advancing our understanding of complex photochemical processes in the troposphere.

In recent years, optical techniques such as Cavity Enhanced Absorption Spectroscopy (CEAS) have developed rapidly. In our previous work, we constructed a compact and lightweight CEAS instrument with high temporal and spatial resolution for precise NO_2 measurements (Zheng et al., 2024). Building upon this foundation, the current study integrates CEAS with the PERCA system, enabling portable and stable detection of ambient RO_2^*. We utilized this system to conduct observations of RO_2^* concentration levels in a coastal area during the autumn. Based on our measurements, the local photochemical $P(O_3)$ was derived and subsequently applied to analyze the influence of transport on O_3 under both clean and polluted conditions.

2 Experiment and methods

The design of our instrument emphasizes a balance between detection performance (e.g., sensitivity and accuracy) and portability in the field. The PERCA-CEAS system consists of two major components: a chemical amplification module and an NO_2 detection module. The former converts trace radicals into detectable NO_2 signals, while the latter provides precise quantification of the generated NO_2. The chemical amplification module adopts a single-channel configuration to reduce system complexity and physical size while maintaining measurement accuracy. Although conventional dual-channel PERCA systems can effectively remove background interferences, they require two NO_2 detectors oper-

ating in parallel (Chen et al., 2016; Liu and Zhang, 2014), leading to potential discrepancy resulted from optical parameters and flow between two channels. In contrast, the single-channel design offers better structural compactness and operational stability. The produced NO_2 concentration is measured by a self-built CEAS system, which features compact size (40 cm × 30 cm × 17 cm) and lightweight design (5.80 kg). Detailed information of CEAS is provided in our previous work (Zheng et al., 2024). The overall structure of the PERCA-CEAS system is presented in Fig. 1.

2.1 Chemical amplification module

The NO and CO gases were injected into the system accompanied by N_2 as a balancing gas. To ensure gas purity, the NO (100 ppmv in N_2) was passed through a ferrous sulfate heptahydrate ($FeSO_4 \cdot 7H_2O$) filter to remove trace NO_2 impurities. The flow rate of this NO mixture was regulated at 120 mL min^{-1}, achieving a final concentration of 8 ppmv in the reactor. Similarly, high-purity CO gas (99.99 %) was passed through an activated carbon column to eliminate residual carbonyl compounds before entering the reactor at 120 mL min^{-1}, corresponding to a constant concentration of 8 % (v/v) during amplification mode. The total system flow was maintained at 1500 mL min^{-1} using mass flow controllers, corresponding to a residence time of approximately 3 s in the reaction zone.

To enable automated switching between amplification and background modes in the single-channel configuration, an automatic valve-switching module driven by a programmable timer was developed. The flow paths of CO and N_2 were controlled using four two-way solenoid valves, with two valves assigned to each gas line. During the amplification mode, the timer directs CO to the front inlet to initiate the chain reaction with NO, while N_2 is routed to the rear inlet. Conversely, in the background mode, the valve states are toggled so that N_2 is introduced at the front and CO is directed to the rear. By synchronizing the switching of these four valves, the system achieves stable and automated mode transitions for real-time detection of peroxy radicals.

Humidity plays a critical role in determining the efficiency of chemical amplification reactions. To control water vapor levels, a Nafion tube dryer (model MD-700-12-F-3, total length 40 cm, effective length 30 cm, ID 1.78 cm) was used to remove water vapor and serve as the chemical amplification reaction chamber in the meantime. To ensure efficient drying and maintain a low-humidity sample stream, a continuous flow of dry purge gas was introduced along the outer side of the Nafion tube. In this work, the dry purge gas was generated by a pump-driven system connected in series with a drying tube filled with indicating silica gel. The gas was first deeply dried through the silica gel column to ensure extremely low moisture content before being circulated from the lower inlet to the upper outlet of the Nafion tube, forming a closed-loop flow. A humidity sensor was installed at the outlet of the sample stream to continuously monitor the relative humidity inside the reaction tube. Through this precise humidity control, the relative humidity during the chemical amplification process was maintained below 20 %, ensuring system stability and improving the reliability of the experimental results.

2.2 Chain length calibration

As described in the principle of the chemical amplification method (Eq. 1), the CL is a key parameter determining the accuracy of peroxy radical measurements. In this work, CL was determined using on-site peroxy radical calibration sources based on water vapor photolysis. A pen-type Hg lamp was used to photolyze H_2O in an N_2 carrier gas (mixture of dry and humidified N_2), producing H atoms and OH radicals (Reaction R5). Immediately downstream of the lamp, a mixture of synthetic air and reagent gases (CO/N_2 or CH_4/N_2) was introduced to allow rapid mixing with the photolysis products and reduce radical wall losses. In this configuration, H atoms react with O_2 in the synthetic air to form HO_2 (Reaction R6), while the reagent gases control the radical composition. When CO is used as the reagent gas, OH radicals are quantitatively converted to HO_2 (Reaction R4), providing a HO_2 calibration source without interference from OH and RO_2 radicals. When CH_4 (150 ppm in N_2) is used instead of CO, OH reacts with CH_4 to form CH_3O_2 (Reaction R7), yielding a mixed peroxy radical source containing approximately 50 % HO_2 and 50 % CH_3O_2 under typical calibration conditions. In all cases, the relative humidity in the calibration flow was adjusted to ∼ 10 %, yielding a stable peroxy radical concentration of ∼ 1–3 ppbv.

$$H_2O + h\nu \rightarrow OH + H \quad \text{(R5)}$$

$$H + O_2 + M \rightarrow HO_2 + M \quad \text{(R6)}$$

$$OH + CH_4 + O_2 + M \rightarrow CH_3O_2 + H_2O + M \quad \text{(R7)}$$

The CL was determined using four distinct NO_2 signals detected by the CEAS. For the pure HO_2 source, the Hg lamp was switched on and CO was introduced immediately behind the H_2O photolysis zone, with NO at the inlet of Nafion reactor. Under these conditions, both H atoms and OH from H_2O photolysis were promptly converted to HO_2, then titrated by NO to form NO_2. The resulting NO_2 signal is denoted as S_1 (amplification mode). In the background mode, the lamp remained on while CO was substituted by N_2. The corresponding NO_2 signal, S_2, represents the background mode when HO_2 is only produced by $H + O_2$ pathway. With the lamp off, signal S_3 and S_4 correspond to the amplification and background signals in the absence of radicals, respectively. Thus, (S_2–S_4) represents the HO_2 only produced by $H + O_2$ pathway, whereas (S_1–S_3) corresponds to the chain-amplified NO_2 signal from HO_2 produced via both the $H+O_2$ and $OH + CO$ pathways. The CL is then obtained from these four signals using Eq. (2). The mixed HO_2–CH_3O_2 standard

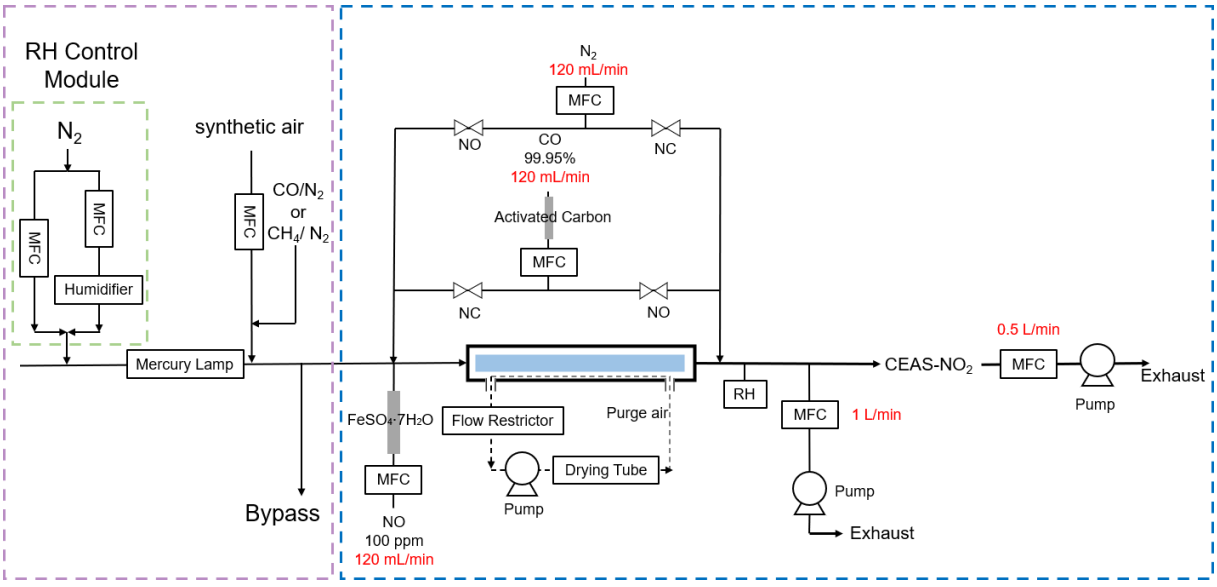

Figure 1. Schematic diagram of the PERCA-CEAS system. The purple dash line portion represents the standard source module, which consists of the standard gas generation unit and the relative humidity (RH) control unit (outlined in green) and is used for calibrating the system chain length. The blue dash line portion represents the measurement module, comprising the chemical amplification unit and the NO_2 detection unit, which together enable the quantification of atmospheric peroxy radicals.

was generated by introducing CH_4 only during the S_1 (amplification) measurement and was used to verify the instrument response to organic peroxy radicals relative to HO_2 under otherwise identical conditions.

$$\mathrm{CL} = \frac{\Delta \mathrm{NO_2}}{[\mathrm{HO_2}]} = \frac{S_1 - S_3}{2(S_2 - S_4)} \tag{2}$$

3 Results and discussion

3.1 Dependence of the CL on Reaction Conditions

The CL is influenced by several factors, including the concentrations of reactive gases, reaction time, relative humidity, and wall losses (Liu and Zhang, 2014). To investigate the response of CL to these parameters in our PERCA-CEAS system, we measured the CL under a series of controlled conditions using a pure HO_2 radical standard source, specifically by varying NO concentrations and RH levels. The CL measurement was repeated at least five times for each condition. For the subsequent experiments, the CO concentration was fixed at 8 %, which is sufficiently high to sustain efficient HO_2 production while remaining within safe limits of CO (explosion range: 12.5 %–74.2 %).

To assess how NO concentration influences CL, we conducted a series of experiments under varying NO levels while keeping the relative humidity fixed at 10 %. As shown in Fig. 2a, CL increases steadily with increasing NO concentration and reaches its maximum when NO is 8 ppm. Considering both measurement efficiency and system economy, 8 ppm was chosen as the optimal NO concentration for instrument operation.

At high RH, water vapor on the reactor walls enhances the heterogeneous uptake of RO_2 and HO_2 and promotes HO_x-terminating reactions, thereby suppressing chain propagation and shortening the CL (Mihele et al., 1999; Yang et al., 2019). To quantify the effect of RH on the CL, a custom-built humidifier was used to control the flow rate of the humidified gas, thereby generating HO_2 sources at different RH levels (10 %–50 %). The relative humidity of the sample gas was monitored by a temperature-humidity sensor installed downstream of the Nafion reaction tube. The experimental results, presented in Fig. 2b, demonstrate a substantial decrease in CL as the RH increases. Specifically, when the relative humidity (RH) of the sample gas passing through the Nafion dryer reaches 50 %, the chain length drops by more than 50.1 %, a reduction that severely compromises the sensitivity required for accurate field RO_2^* measurements. Consequently, to ensure optimal measurement performance, the RH of the airflow entering the amplification zone is strictly controlled to remain below 20 % during field campaigns, corresponding to 45 % RH in ambient air.

The optimal CL for the PERCA-CEAS measurement system was determined to be 30 ± 2 under the conditions of RH = 10 %, NO = 8 ppm, and CO = 8 % based on the pure HO_2 calibration. Calibration using a mixed radical source consisting of 50 % HO_2 and 50 % CH_3O_2 yielded a CL of 24 ± 1 under the same conditions. As summarized in Table 1, the obtained CL is lower than values reported in most previous PERCA studies, which were typically above 50

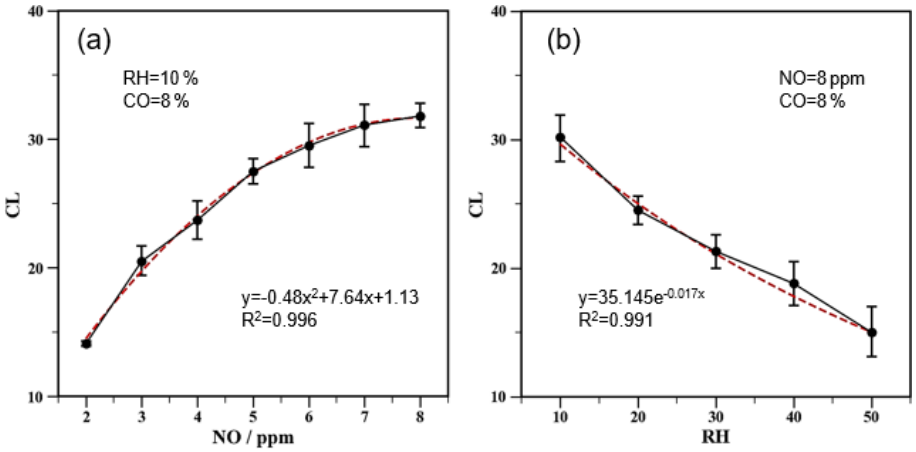

Figure 2. **(a)** Relationship between the CL and NO concentration under conditions of 10 % RH and 8 % CO concentration. **(b)** Variation of CL with RH at a fixed NO concentration of 8 ppm and CO concentration of 8 %. (Error bars represent the standard deviation of five independent measurements.)

and occasionally exceeded 200 (George et al., 2020; Wood and Charest, 2014). The differences in CL are primarily attributed to wall loss of HO_2 radicals due to reactor material, reactor design and working pressure. Although the obtained CL is relatively low compared with these PERCA instruments, the results demonstrate that the developed PERCA-CEAS system provides stable and reliable sensitivity for atmospheric RO_2^* measurements.

3.2 Detection Limit and Measurement Uncertainty

In the PERCA–CEAS system, the concentration of RO_2^* is determined by converting it into measurable NO_2 through chain reactions with excess NO. Consequently, the overall detection limit of the system depends on both the detection limit of NO_2 and the CL, as described by Eq. (3). The LOD for the CEAS-NO_2 detector was determined under laboratory conditions by continuously measuring high-purity zero-air for over 5 h and calculating the standard deviation of blank noise (Zheng et al., 2024). At a 3 min time resolution, the LOD of NO_2 was determined to be 11.4 pptv, corresponding to a detection limit of 0.38 pptv (1σ, 3 min) for RO_2^*, based on a CL of 30 derived from the pure HO_2 calibration.

The overall measurement uncertainty of the system was quantified using the Gaussian error propagation (Eq. 4). Four major sources contribute to the total uncertainty: (1) NO_2 measurement uncertainty (6 %), which includes uncertainties in the absorption cross-section (4 %), mirror reflectivity calibration (5 %), effective cavity length (0.5 %), and pressure measurement (0.1 %). (2) CL calibration uncertainty (6.7 %), derived from repeated calibration results (30 ± 2). (3) Uncertainty in radical partitioning. This arises from variability in the relative contributions of HO_2 and CH_3O_2 to total peroxy radicals. Based on the reported HO_2/RO_2 (0.8–1.2) and CH_3O_2/RO_2 (0.85–0.95) ratios from Stone et al. (2010), the mole fraction of CH_3O_2 in total peroxy radicals (f) is estimated to be 0.41–0.54. Under these conditions, the use of an HO_2-based calibration would introduce a systematic bias of 16 %–22 % in the derived RO_2^* concentration. (4) PAN interference. The thermal decomposition of PAN represents a potential source of interference, as it releases NO_2 and peroxy radicals that can trigger additional chemical amplification within the reactor (Liu and Zhang, 2014; Wood and Charest, 2014). Kinetic simulations using the F0AM model (Framework for 0-D Modeling; Wolfe et al., 2016) indicate that 1.0 ppbv PAN results in an equivalent RO_2^* signal of 1.95 pptv under our experimental conditions (26.5 °C and an amplification reaction time of 0.15 s). This accounts for 1.3 %–9.8 % of the typical RO_2^* levels (20–150 pptv) observed during the campaign. Based on these factors, the overall uncertainty in RO_x measurement was estimated to be 18.4 %–25.7 %, demonstrating the robustness and reliability of the PERCA–CEAS system for RO_2^* measurement.

$$\mathrm{LOD}\left(\mathrm{RO_2^*}\right) = \frac{\mathrm{LOD}(\mathrm{NO_2})}{\mathrm{CL}} \tag{3}$$

$$\frac{\sigma_{\mathrm{RO_2^*}}}{\left[\mathrm{RO_2^*}\right]} = \sqrt{\left(\frac{\sigma_{\mathrm{NO_2}}}{[\mathrm{NO_2}]}\right)^2 + \left(\frac{\sigma_{\mathrm{CL}}}{\mathrm{CL}}\right)^2 + \left(\frac{\sigma_{\mathrm{Part}}}{\mathrm{Part}}\right)^2 + \left(\frac{\sigma_{\mathrm{PAN}}}{\mathrm{PAN}}\right)^2} \tag{4}$$

3.3 Field Observation of RO_2^*

The instrument has been deployed in a field campaign to evaluate the performance of instrument under real atmospheric conditions. All instruments are placed on the roof of a six-story building on the campus of Sun Yat-sen University (22°21′06″ N, 113°35′42″ E), which is located on the western shore of the Pearl River Estuary and approximately 15 km from downtown Zhuhai. The observation site mainly

Table 1. Summary of performance for reported PERCA measurement systems.

Measurement System	Channel Configuration	Calibration Source	CL	LOD	Uncertainty	Pressure (mbar)	Reference
PERCA-luminox	Single	CH_3O_2	200–260	2 pptv	40 %	400–1000	Green et al. (2003)
PERCA-luminol	Dual	HO_2 50 % HO_2 + 50 % CH_3O_2	45 ± 7	3 ± 2 pptv (3σ)	/	200	Kartal et al. (2010)
PERCA-luminol	Dual	HO_2 50 % HO_2 + 50 % CH_3O_2	88 ± 17 64 ± 18	3 pptv (1σ)	/	300	Horstjann et al. (2014)
PERCA-CRDS	Dual	HO_2	150 ± 50	10 pptv (3σ)	/	1000	Liu et al. (2009)
PERCA-CRDS	Dual	HO_2 CH_3O_2	200 180	4 pptv (3σ)	/	1000	Liu and Zhang (2014)
PERCA-CRDS	Dual	HO_2 50 % HO_2 + 50 % CH_3O_2	62 ± 9	< 2 pptv	15 %	200–350	George et al. (2020)
PERCA-CRDS	Dual	HO_2 RO_2^*	55	0.9 pptv (3σ)	/	1000	Duncianu et al. (2020)
PERCA-CAPS	Dual	$CH_3C(O)O_2$ CH_3O_2	168 ± 20	0.6 pptv (1σ, 60 s)	25 %	1000	Wood and Charest (2014)
ECHAMP-CAPS	Dual	$CH_3C(O)O_2$ CH_3O_2	17	2.5 pptv (1σ, 90 s)	27 %	1000	Wood et al. (2017)
PERCA-IBBCEAS	Dual	HO_2	91 ± 11	0.9 pptv (1σ)	16 %–20 %	1000	Chen et al. (2016)
PERCA-CEAS	Single	HO_2 50 % HO_2 + 50 % CH_3O_2	30 ± 2 24 ± 1	0.38 pptv (1σ)	18.4 %–25.7 %	1000	This work

received an airmass mixed with vehicle emissions from a traffic artery (~ 300 m) and nearby residential areas. There are no major industrial facilities in the surroundings.

The field observation campaign was conducted from 26 October to 15 November 2024, producing more than 15 d of valid continuous RO_2^* radical data. For PERCA-CEAS operation, both the chemical amplification mode and the background mode were set to 90 s in this observation, resulting in a time resolution of 3 min. Ambient temperature and relative humidity were continuously monitored using a temperature-humidity probe (HC2A-SH, ROTRONIC, Switzerland). The concentrations of NO and NO_2 were measured by a commercial chemiluminescence analyzer (Model 42i-TL, Thermo, USA), while O_3 concentrations were obtained using a UV photometric analyzer (Model 49i, Thermo, USA). The mirror reflectivity of the CEAS detector was calibrated before and after the campaign, and the results remained consistent.

Figure 3a–c presents the time series of meteorological parameters and major pollutants during the observation period. Ambient temperature was consistently above 25 °C, with an average value of 28.44 ± 1.5 °C. Due to the coastal meteorological conditions, the RH was relatively high and showed clear diurnal variations – lower during the day and higher at night – ranging from 25 % to 85 %, with an average of 55.98 % ± 12.53 %. Low NO and NO_2 concentrations were observed with an average of 0.34 ± 0.81 ppbv and 13.21 ± 4.72 ppbv, respectively, indicating generally weak NO_x emissions from traffic at this site. The daily maximum of O_3 concentrations ranged from 54 to 116 ppbv, while the overall mean concentration was 44.86 ± 25.03 ppbv, suggesting a moderate level of photochemical pollution during the observation period.

Compared to previous observations in PRD region, moderate levels of RO_2^* were observed with the daily peaks ranging from 48 to 87 pptv (Fig. 3d). The RO_2^* exhibited a pronounced daytime peak, with an average of 51.3 pptv at around 13:00 LT, and decreased to around 20 pptv at night (Fig. 4a). The relatively high level of RO_2^* at night indicates the presence of a nighttime peroxy radical source possibly due to NO_3 chemistry oxidation. We found that the average NO_3 production rate ($P(NO_3)$) at night during the campaign was approximately 1.4 ppbv h^{-1}, higher than the reported warm-season mean of 1.07 ± 0.38 ppbv h^{-1} over China (Wang et al., 2023a), indicating active nighttime NO_3 chemistry at this site. The daytime average of RO_2^* (31.11 pptv) was 1–3 times higher than those reported in most suburban areas, while it was lower than those observed in urban areas (Tan et al., 2019; Wang et al., 2023b).

In addition, our observed RO_2^* exhibited nonlinear response to NO variation (Fig. 4b). At low NO levels, RO_2^*

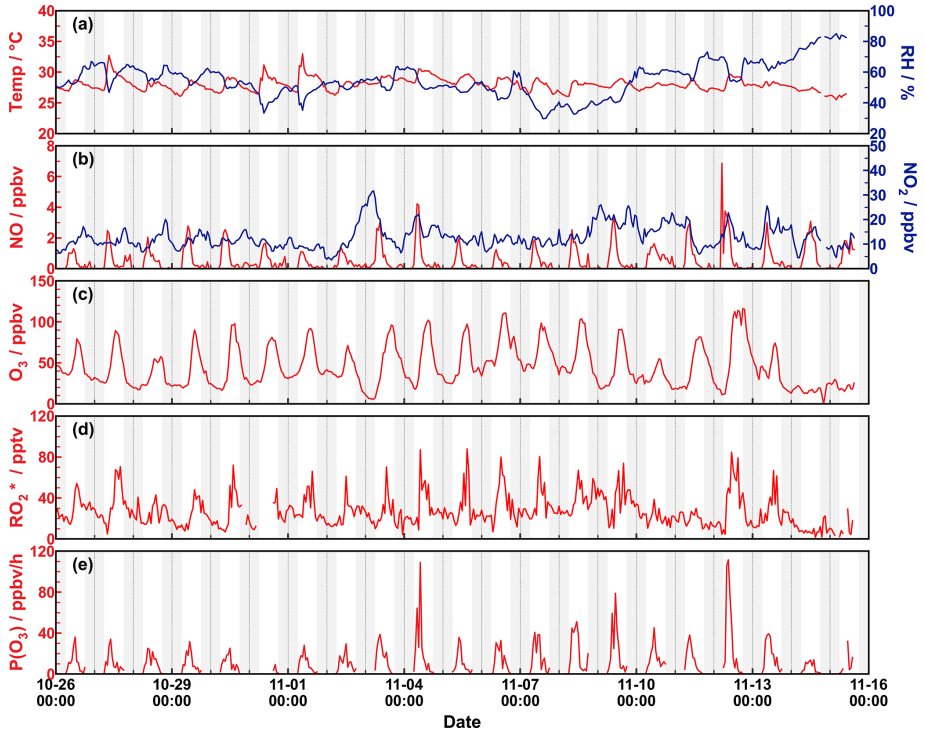

Figure 3. Time series of meteorological parameters (T, RH), major pollutants (O_3, NO_x, RO_2^*), and daytime $P(O_3)$ (06:00–18:00) during the autumn observation period of 2024, with a temporal resolution of 1 h.

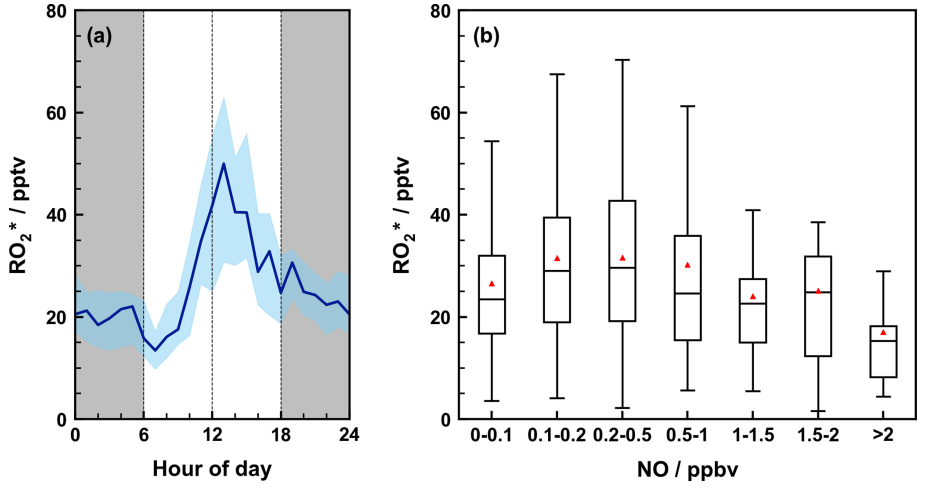

Figure 4. Diurnal variation of RO_2^* and its dependence on NO concentration. **(a)** Average diurnal variation of RO_2^* during the observation period. The gray shaded areas indicate nighttime (18:00–06:00), the dark line represents the median values, and the light blue shading shows the interquartile range (25th–75th percentile). **(b)** Boxplots of RO_2^* distributions under different NO concentration ranges. The black line inside each box denotes the median, and the red triangles indicate the mean RO_2^* values for each NO interval.

increases with NO by promoting the RO_2^*–HO_x propagation cycle. Once NO exceeds about 1 ppbv, the excess NO rapidly converts peroxy radicals into termination products (e.g., organic nitrates), thus interrupting the radical chain cycle and leading to a decline in RO_2^* concentrations (Thornton et al., 2002). The turning point of NO response is higher than that reported in previous studies (Ma et al., 2022; Wei et al., 2023; Yang et al., 2022). This behavior is consistent with the elevated VOC reactivity inferred for studies conducted near our observation site. Studies at nearby coastal sites (e.g., Da Wan Shan Island) have reported high oxidative capacity associated with strong VOC consumption and enhanced radical

cycling (Sun et al., 2024), while the dense vegetation in the Pearl River Delta contributes substantial biogenic VOC emissions (e.g., isoprene) (Situ et al., 2013; Wang et al., 2023c). Collectively, these factors contribute to sustaining propagation cycles of RO_2 radical and shift the turning point of the NO dependence of RO_2^* concentration higher at our site.

3.4 Local production and Transport of Ozone

The instantaneous ozone production rate is driven by peroxy radical chain propagation involving the reaction of NO and RO_2^* (Griffith et al., 2016). Therefore, we calculated $P(O_3)$ based on measured RO_2^* using Eq. (5). Since the rate constants of HO_2 + NO and RO_2 + NO reactions are similar (the difference between k_{NO+HO_2} and k_i is less than 10 %) (Orlando and Tyndall, 2012), an effective rate constant k_{eff} is adopted for the calculation, which is typically approximated by the value of k_{NO+HO_2} (Anderson et al., 2019). The photochemical loss of ozone $D(O_3)$ is calculated using Eq. (6), including the photolysis, reactions with OH and HO_2, and the reaction of NO_2 with OH (Tan et al., 2021). Here, $D(O_3)$ was derived using kinetic rate constants together with observed mean concentrations (and representative literature values for unmeasured species) under 298 K and 1 atm. Using the typical conditions ($j(O^1D) = 1.0 \times 10^{-5}\,s^{-1}$, $OH = 1.0 \times 10^6\,cm^{-3}$, NO = 10 ppbv, O_3 = 40 ppbv, $HO_2 \approx 15$ pptv), $D(O_3)$ was estimated to be $\sim 0.70\,ppbv\,h^{-1}$, accounting for only ~ 5 % of $P(O_3)$. Therefore, $P(O_3)$ can be approximated as $P(O_3)_{net}$. Considering uncertainties associated with RO_2^* measurements (18.4 %–25.7 %), the approximation of k_{eff} (~ 10 %), and upper limit of $D(O_3)$ level (5 %), the overall uncertainty in $P(O_3)_{net}$ was estimated to be 21.5 %–28.0 %.

$$P(O_3) = k_{NO+HO_2}[HO_2][NO] + [NO]\sum_i k_i[RO_2]_i = k_{eff}[RO_2^*][NO] \quad (5)$$

$$D(O_3) = f_{H_2O}\,j(O^1D)[O_3] + k_{OH+O_3}[OH][O_3] + k_{HO_2+O_3}[HO_2][O_3] + k_{OH+NO_2}[OH][NO_2] \quad (6)$$

$$P(O_3)_{net} = P(O_3) - D(O_3) \quad (7)$$

Substantial variability in $P(O_3)$ was observed during the campaign, with daily peak values ranging from 14 to 111 $ppbv\,h^{-1}$ and a daytime average of $14.41 \pm 17.04\,ppbv\,h^{-1}$ (Fig. 3e). After sunrise, with increasing solar intensity and NO concentrations, photochemical reactions became more active, leading to a rapid increase in $P(O_3)$, which peaked around 10:00 ($\sim 27\,ppbv\,h^{-1}$) (Fig. 5a). Subsequently, $P(O_3)$ gradually decreased in the afternoon with the weakening solar radiation. We found a sustaining increase of $P(O_3)$ with NO concentration (Fig. 5b), suggesting that ozone formation fell within the NO_x-limited regime under typical daytime conditions at this site. Similar positive $P(O_3)$–NO_x relationships have been reported in both urban and suburban environments – such as the Nashville plume study (Thornton et al., 2002), rural North China field campaigns (Tan et al., 2018a), and recent observations in Hefei (Yu et al., 2023). The consistent increase of $P(O_3)$ and RO_2^* within low NO_x levels demonstrates that the chain propagation for peroxy formation can be enhanced by NO increase and jointly accelerate instantaneous $P(O_3)$.

We summarized previously reported observations of RO_2^*, $P(O_3)$, and related parameters in Table 2. The $P(O_3)$ observed in this study was generally higher than those at low-NO sites such as Wangdu ($10.44\,ppbv\,h^{-1}$), San Antonio ($4.2\,ppbv\,h^{-1}$), and Hefei ($5.91\,ppbv\,h^{-1}$) except for a suburban site in northern China ($19.5\,ppbv\,h^{-1}$). Even high-NO sites like Paris ($15.8\,ppbv\,h^{-1}$) and Heshan ($18.1\,ppbv\,h^{-1}$) showed comparable or slightly higher $P(O_3)$ than our results. This comparison suggests that, despite the moderate RO_2^* levels at our site, the instantaneous photochemical ozone production remained considerably strong, pointing to an efficient RO_2^*–NO_x catalytic cycle in Zhuhai.

Based on our measurements, we can quantitatively distinguish the relative contributions from local photochemical production and regional transport to surface O_3. Considering the rapid equilibrium between NO_2 and O_3, the variation of odd oxidants ($d[O_x]/dt$, where $O_x = O_3 + NO_2$) is used to reflect the combined influence of local photochemical and transport on surface ozone. Therefore, the transport impact can be expressed by $R(O_3)$, which is calculated from the difference between $d[O_x]/dt$ and $P(O_3)_{net}$ as defined in Eq. (8):

$$R(O_3) = \frac{dO_x}{dt} - P(O_3)_{net} \quad (8)$$

Here, the sign of $R(O_3)$ indicates the different influences from transport. When $R(O_3) > 0$, regional transport enhances local O_3 concentrations, suggesting that O_3 could be contributed by transport from surrounding regions. Conversely, $R(O_3) < 0$ implies that transport acts as a dilution or export role in regulating the surface ozone.

The contribution from local photochemical production and transport to surface O_3 exhibited distinct patterns under different pollution conditions (Fig. 6). We define the polluted days as the maximum O_3 concentration exceeding the national Class I standard of $160\,\mu g\,m^{-3}$, while the clean periods corresponded to days with a maximum hourly O_3 concentration below $120\,\mu g\,m^{-3}$. A total of 14 d and 4 d are categorized into polluted and clean periods, respectively. The daytime increase in ozone concentration in Zhuhai was primarily driven by local photochemical production, whereas regional transport generally exhibited an export effect. However, the magnitudes and temporal patterns of their contributions differed significantly between clean and pollution scenarios. The $P(O_3)$ exhibited similar diurnal variations among both polluted and clean days, while polluted periods showed stronger ozone formation than clean periods. Specifically, the peak $P(O_3)$ on polluted days reached $\sim 30\,ppbv\,h^{-1}$, which was approximately 50 % higher than that on clean days ($\sim 20\,ppbv\,h^{-1}$). In contrast to $P(O_3)$, the behavior of $R(O_3)$ on

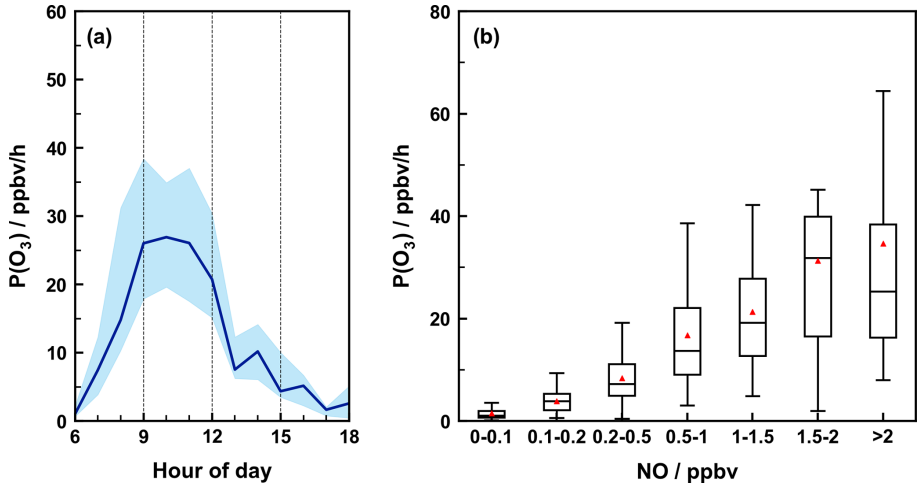

Figure 5. Diurnal variation and NO-dependent distribution of daytime $P(O_3)$. **(a)** Average diurnal profile of daytime $P(O_3)$ during the observation period. The dark line denotes the median, and the light blue shading indicates the interquartile range (25th–75th percentile). **(b)** Box plots of daytime $P(O_3)$ under different NO concentration ranges. The black line inside each box represents the median, and the red triangle marks the mean value within each interval.

Table 2. Summary of observed RO_2^*, HO_2, NO, O_3, and $P(O_3)$ during the field campaign.

Region	Location	Season, year	RO_2^* (pptv)	HO_2 (pptv)	NO (ppbv)	O_3 (ppbv)	$P(O_3)$ (ppbv h^{-1})	References
Suburban	Paris, France	Summer, 2009	5.6	/	4	38	15.8[d]	(Michoud et al., 2012)
Rural	Wangdu, China	Summer, 2014	43.23[a]	19.52[a]	0.72[a]	72.37[a]	10.44[a,c]	(Tan et al., 2017)
Suburban	Heshan, China	Autumn, 2014	17.1	10.2	2.5	42.5	18.1[c]	(Tan et al., 2019)
Urban	San Antonio, USA	Summer, 2017	37[b]	/	0.23[b]	40[b]	4.2[b,c]	(Anderson et al., 2019)
Urban	Guangzhou, China	Autumn, 2018	91.5	/	4.31	31.6	/	(Wang et al., 2023b)
Suburban	Hefei, China	Summer, 2020	27.62	/	0.37	55.19	5.91[c]	(Yu et al., 2023)
Suburban	Huaibei, China	Autumn, 2021	50.34	/	0.3	52.66	19.5[d]	(Wei et al., 2023)
Coastal	Zhuhai, China	Autumn, 2024	31.11	/	0.84	54.44	14.41[c]	This work

Note: All unmarked data represent daytime averages (06:00–18:00).
[a] indicates daytime median values (06:00–16:00);
[b] indicates daytime median values (07:00–20:00);
[c] represents $P(O_3)$ calculated based on the observed peroxy radical concentrations;
[d] represents $P(O_3)$ calculated based on model-simulated peroxy radicals;
"/" represents data not available.

polluted days diverged significantly from that on clean days. Around midday, $R(O_3)$ on polluted days rose rapidly from a negative value to zero and became slightly positive, indicating a suppressed airmass dispersion or even slight import from regional O_3. The distinct transport patterns during polluted days are attributed to frequent coastal wind-field convergence that weakened ventilation. Such weakening export in the midday facilitated the rapid accumulation of locally produced ozone and contributed to the higher O_3 peaks during polluted days compared to clean days. As a result, the elevated surface ozone on polluted days was resulted from the combined effect of stronger photochemical production and reduced O_3 export at midday, whereas the $P(O_3)$ was almost offset by the transport effect of O_3 on clean days, leading to flat variation of O_3.

4 Conclusions

This study combined the PERCA technique with CEAS to develop a single-channel PERCA–CEAS system. The system enables real-time, online measurements of RO_2^*, providing a robust technical support for evaluating atmospheric oxidation capacity and elucidating tropospheric photochemical mechanisms. Experimental investigations were conducted to determine key parameters affecting measurement performance. The detection limit for RO_2^* was 0.38 pptv (1σ) at a time resolution of 3 min, with an overall measurement uncertainty of 18.4 %–25.7 %, demonstrating high sensitivity and stability that meet the requirements for field observations of ambient RO_2^*. Our PERCA–CEAS system was successfully deployed for ambient measurement and found moderate RO_2^* levels

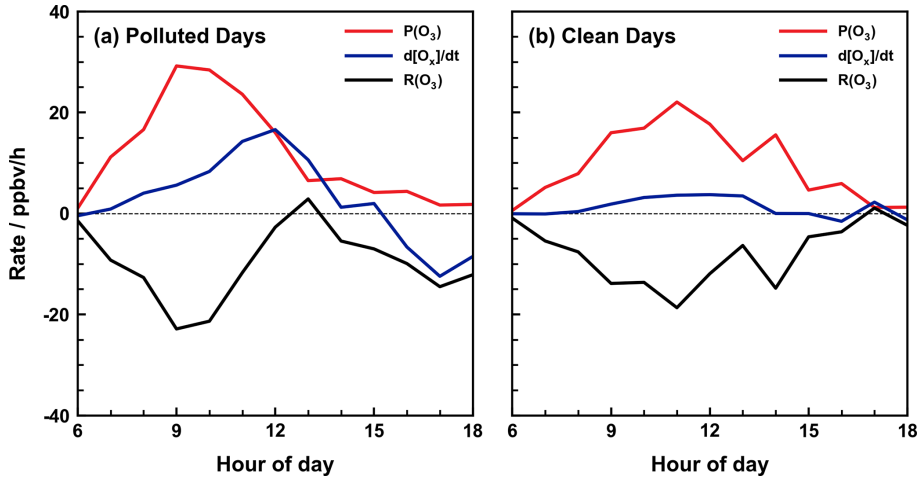

Figure 6. Diurnal variations of daytime $P(O_3)$, $d[O_x]/dt$, and $R(O_3)$ during **(a)** polluted and **(b)** clean periods. The red line represents the photochemical ozone production rate $P(O_3)$, the blue line indicates the rate of change of total oxidants $d[O_x]/dt$, and the black line corresponds to the regional transport rate $R(O_3)$.

in a coastal area. The $P(O_3)$ derived from measured RO_2^* was further used to evaluate the O_3 formation regime and transport influence on O_3. The higher O_3 levels observed on polluted days compared to clean days were driven by both stronger photochemical production and reduced export effects during midday in this coastal area. Our study, therefore, provides an important reference for extending the peroxy radical measurement techniques to quantify in-situ formation and transport of O_3. We also suggest more field observations of peroxy radicals in diverse environments to support the strategy formulation of O_3 pollution.

Data availability. The dataset is available at https://doi.org/10.5281/zenodo.18346203 (Tang et al., 2026).

Author contributions. X.R.C. and H.C.W. conceived the study. R.J.T., and Z.L.Z., H.C.W. and X.R.C. analyzed the data and wrote the manuscript. R.J.T., Z.L.Z. set up the instrument and conducted the field experiment with the help of H.X.L. and Y.M.W. All authors contributed to the results and commented on the manuscript.

Competing interests. The contact author has declared that none of the authors has any competing interests.

Disclaimer. Publisher's note: Copernicus Publications remains neutral with regard to jurisdictional claims made in the text, published maps, institutional affiliations, or any other geographical representation in this paper. The authors bear the ultimate responsibility for providing appropriate place names. Views expressed in the text are those of the authors and do not necessarily reflect the views of the publisher.

Financial support. This research has been supported by the National Key Research and Development Program of China (grant no. 2023YFC3710900), the Foundation for Distinguished Young Talents in Higher Education of Guangdong (grant no. 2024B1515020075), and the National Natural Science Foundation of China (grant no. 22576242).

Review statement. This paper was edited by María Cazorla and reviewed by two anonymous referees.

References

Anderson, D. C., Pavelec, J., Daube, C., Herndon, S. C., Knighton, W. B., Lerner, B. M., Roscioli, J. R., Yacovitch, T. I., and Wood, E. C.: Characterization of ozone production in San Antonio, Texas, using measurements of total peroxy radicals, Atmos. Chem. Phys., 19, 2845–2860, https://doi.org/10.5194/acp-19-2845-2019, 2019.

Cantrell, C. A., Shetter, R. E., and Calvert, J.: Peroxy radical chemistry during FIELDVOC 1993 in brittany, france, Atmos. Environ., 30, 3947–3957, https://doi.org/10.1016/1352-2310(96)00136-7, 1996.

Chen, T., Zhang, P., Chu, B., Ma, Q., Ge, Y., Liu, J., and He, H.: Secondary organic aerosol formation from mixed volatile organic compounds: effect of RO_2 chemistry and precursor concentration, npj Clim. Atmos. Sci., 5, 95–103, https://doi.org/10.1038/s41612-022-00321-y, 2022.

Chen, Y., Yang, C., Zhao, W., Fang, B., Xu, X., Gai, Y., Lin, X., Chen, W., and Zhang, W.: Ultra-sensitive measurement of peroxy radicals by chemical amplification broadband cavity-enhanced spectroscopy, Analyst, 141, 5870–5878, https://doi.org/10.1039/C6AN01038E, 2016.

Duncianu, M., Lahib, A., Tomas, A., Stevens, P. S., and Dusanter, S.: Characterization of a chemical amplifier for peroxy radical

measurements in the atmosphere, Atmos. Environ., 222, 117106, https://doi.org/10.1016/j.atmosenv.2019.117106, 2020.

Edwards, G. D., Cantrell, C. A., Stephens, S., Hill, B., Goyea, O., Shetter, R. E., Mauldin, R. L., Kosciuch, E., Tanner, D. J., and Eisele, F. L.: Chemical ionization mass spectrometer instrument for the measurement of tropospheric HO_2 and RO_2, Anal. Chem., 75, 5317–5327, https://doi.org/10.1021/ac034402b, 2003.

Ehn, M., Thornton, J. A., Kleist, E., Sipilä, M., Junninen, H., Pullinen, I., Springer, M., Rubach, F., Tillmann, R., Lee, B., Lopez-Hilfiker, F., Andres, S., Acir, I.-H., Rissanen, M., Jokinen, T., Schobesberger, S., Kangasluoma, J., Kontkanen, J., Nieminen, T., Kurtén, T., Nielsen, L. B., Jørgensen, S., Kjaergaard, H. G., Canagaratna, M., Maso, M. D., Berndt, T., Petäjä, T., Wahner, A., Kerminen, V.-M., Kulmala, M., Worsnop, D. R., Wildt, J., and Mentel, T. F.: A large source of low-volatility secondary organic aerosol, Nature, 506, 476–479, https://doi.org/10.1038/nature13032, 2014.

Gao, Y., Lu, K., and Zhang, Y.: Review of technologies and their applications for the speciated detection of RO_2 radicals, J. Environ. Sci., 123, 487–499, https://doi.org/10.1016/j.jes.2022.09.028, 2023.

George, M., Andrés Hernández, M. D., Nenakhov, V., Liu, Y., and Burrows, J. P.: Airborne measurement of peroxy radicals using chemical amplification coupled with cavity ring-down spectroscopy: the PeRCEAS instrument, Atmos. Meas. Tech., 13, 2577–2600, https://doi.org/10.5194/amt-13-2577-2020, 2020.

Green, T. J., Reeves, C. E., Brough, N., Edwards, G. D., Monks, P. S., and Penkett, S. A.: Airborne measurements of peroxy radicals using the PERCA technique, J. Environ. Monitor, 5, 75–83, https://doi.org/10.1039/b204493e, 2003.

Griffith, S. M., Hansen, R. F., Dusanter, S., Michoud, V., Gilman, J. B., Kuster, W. C., Veres, P. R., Graus, M., De Gouw, J. A., Roberts, J., Young, C., Washenfelder, R., Brown, S. S., Thalman, R., Waxman, E., Volkamer, R., Tsai, C., Stutz, J., Flynn, J. H., Grossberg, N., Lefer, B., Alvarez, S. L., Rappenglueck, B., Mielke, L. H., Osthoff, H. D., and Stevens, P. S.: Measurements of hydroxyl and hydroperoxy radicals during CalNex-LA: model comparisons and radical budgets, J. Geophys. Res.-Atmos., 121, 4211–4232, https://doi.org/10.1002/2015JD024358, 2016.

Hornbrook, R. S., Crawford, J. H., Edwards, G. D., Goyea, O., Mauldin III, R. L., Olson, J. S., and Cantrell, C. A.: Measurements of tropospheric HO_2 and RO_2 by oxygen dilution modulation and chemical ionization mass spectrometry, Atmos. Meas. Tech., 4, 735–756, https://doi.org/10.5194/amt-4-735-2011, 2011.

Horstjann, M., Andrés Hernández, M. D., Nenakhov, V., Chrobry, A., and Burrows, J. P.: Peroxy radical detection for airborne atmospheric measurements using absorption spectroscopy of NO_2, Atmos. Meas. Tech., 7, 1245–1257, https://doi.org/10.5194/amt-7-1245-2014, 2014.

Kartal, D., Andrés-Hernández, M. D., Reichert, L., Schlager, H., and Burrows, J. P.: Technical Note: Characterisation of a DUALER instrument for the airborne measurement of peroxy radicals during AMMA 2006, Atmos. Chem. Phys., 10, 3047–3062, https://doi.org/10.5194/acp-10-3047-2010, 2010.

Liang, W., Yu, H., Xu, H., Wang, Z., Li, T., Feng, Y., Russell, A., and Shi, G.: Probing into ozone production through photochemistry of organic peroxyl radicals: implications for source control, J. Geophys. Res.-Atmos., 129, e2023JD040124, https://doi.org/10.1029/2023JD040124, 2024.

Liu, Y. and Zhang, J.: Atmospheric peroxy radical measurements using dual-channel chemical amplification cavity ringdown spectroscopy, Anal. Chem., 86, 5391–5398, https://doi.org/10.1021/ac5004689, 2014.

Liu, Y., Morales-Cueto, R., Hargrove, J., Medina, D., and Zhang, J.: Measurements of peroxy radicals using chemical amplification-cavity ringdown spectroscopy, Environ. Sci. Technol., 43, 7791–7796, https://doi.org/10.1021/es901146t, 2009.

Lou, S., Tan, Z., Gan, G., Chen, J., Wang, H., Gao, Y., Huang, D., Huang, C., Li, X., Song, R., Wang, H., Wang, M., Wang, Q., Wu, Y., and Huang, C.: Observation based study on atmospheric oxidation capacity in shanghai during late-autumn: contribution from nitryl chloride, Atmos. Environ., 271, 118902, https://doi.org/10.1016/j.atmosenv.2021.118902, 2022.

Lu, K. D., Rohrer, F., Holland, F., Fuchs, H., Bohn, B., Brauers, T., Chang, C. C., Häseler, R., Hu, M., Kita, K., Kondo, Y., Li, X., Lou, S. R., Nehr, S., Shao, M., Zeng, L. M., Wahner, A., Zhang, Y. H., and Hofzumahaus, A.: Observation and modelling of OH and HO_2 concentrations in the Pearl River Delta 2006: a missing OH source in a VOC rich atmosphere, Atmos. Chem. Phys., 12, 1541–1569, https://doi.org/10.5194/acp-12-1541-2012, 2012.

Ma, X., Tan, Z., Lu, K., Yang, X., Liu, Y., Li, S., Li, X., Chen, S., Novelli, A., Cho, C., Zeng, L., Wahner, A., and Zhang, Y.: Winter photochemistry in beijing: observation and model simulation of OH and HO_2 radicals at an urban site, Sci. Total Environ., 685, 85–95, https://doi.org/10.1016/j.scitotenv.2019.05.329, 2019.

Ma, X., Tan, Z., Lu, K., Yang, X., Chen, X., Wang, H., Chen, S., Fang, X., Li, S., Li, X., Liu, J., Liu, Y., Lou, S., Qiu, W., Wang, H., Zeng, L., and Zhang, Y.: OH and HO_2 radical chemistry at a suburban site during the EXPLORE-YRD campaign in 2018, Atmos. Chem. Phys., 22, 7005–7028, https://doi.org/10.5194/acp-22-7005-2022, 2022.

Michoud, V., Kukui, A., Camredon, M., Colomb, A., Borbon, A., Miet, K., Aumont, B., Beekmann, M., Durand-Jolibois, R., Perrier, S., Zapf, P., Siour, G., Ait-Helal, W., Locoge, N., Sauvage, S., Afif, C., Gros, V., Furger, M., Ancellet, G., and Doussin, J. F.: Radical budget analysis in a suburban European site during the MEGAPOLI summer field campaign, Atmos. Chem. Phys., 12, 11951–11974, https://doi.org/10.5194/acp-12-11951-2012, 2012.

Mihelcic, D., Müsgen, P., and Ehhalt, D. H.: An improved method of measuring tropospheric NO_2 and RO_2 by matrix isolation and electron spin resonance, J. Atmos. Chem., 3, 341–361, https://doi.org/10.1007/BF00122523, 1985.

Mihelcic, D., Volz-Thomas, A., Pätz, H. W., Kley, D., and Mihelcic, M.: Numerical analysis of ESR spectra from atmospheric samples, J. Atmos. Chem., 11, 271–297, https://doi.org/10.1007/BF00118353, 1990.

Mihele, C. M., Mozurkewich, M., and Hastie, D. R.: Radical loss in a chain reaction of CO and NO in the presence of water: implications for the radical amplifier and atmospheric chemistry, Int. J. Chem. Kinet., 31, 145–152, https://doi.org/10.1002/(SICI)1097-4601(1999)31:2%3C145::AID-KIN7%3E3.0.CO;2-M, 1999.

Monks, P. S.: Gas-phase radical chemistry in the troposphere, Chem. Soc. Rev., 34, 376, https://doi.org/10.1039/b307982c, 2005.

Orlando, J. J. and Tyndall, G. S.: Laboratory studies of organic peroxy radical chemistry: an overview with emphasis on recent issues of atmospheric significance, Chem. Soc. Rev., 41, 6294, https://doi.org/10.1039/c2cs35166h, 2012.

Reichert, L., Andrés Hernández, M. D., Stöbener, D., Burkert, J., and Burrows, J. P.: Investigation of the effect of water complexes in the determination of peroxy radical ambient concentrations: implications for the atmosphere, J. Geophys. Res.-Atmos., 108, https://doi.org/10.1029/2002JD002152, 2003.

Situ, S., Guenther, A., Wang, X., Jiang, X., Turnipseed, A., Wu, Z., Bai, J., and Wang, X.: Impacts of seasonal and regional variability in biogenic VOC emissions on surface ozone in the Pearl River delta region, China, Atmos. Chem. Phys., 13, 11803–11817, https://doi.org/10.5194/acp-13-11803-2013, 2013.

Sommariva, R., Brown, S. S., Roberts, J. M., Brookes, D. M., Parker, A. E., Monks, P. S., Bates, T. S., Bon, D., de Gouw, J. A., Frost, G. J., Gilman, J. B., Goldan, P. D., Herndon, S. C., Kuster, W. C., Lerner, B. M., Osthoff, H. D., Tucker, S. C., Warneke, C., Williams, E. J., and Zahniser, M. S.: Ozone production in remote oceanic and industrial areas derived from ship based measurements of peroxy radicals during TexAQS 2006, Atmos. Chem. Phys., 11, 2471–2485, https://doi.org/10.5194/acp-11-2471-2011, 2011.

Stone, D., Evans, M. J., Commane, R., Ingham, T., Floquet, C. F. A., McQuaid, J. B., Brookes, D. M., Monks, P. S., Purvis, R., Hamilton, J. F., Hopkins, J., Lee, J., Lewis, A. C., Stewart, D., Murphy, J. G., Mills, G., Oram, D., Reeves, C. E., and Heard, D. E.: HO_x observations over West Africa during AMMA: impact of isoprene and NO_x, Atmos. Chem. Phys., 10, 9415–9429, https://doi.org/10.5194/acp-10-9415-2010, 2010.

Sun, J., Yu, X., Ling, Z., Fang, G., Ming, L., Zhao, J., Zou, S., Guan, H., Wang, H., Wang, X., Wang, Z., Gao, Y., Tham, Y. J., Guo, H., and Zhang, Y.: Roles of photochemical consumption of VOCs on regional background O3 concentration and atmospheric reactivity over the pearl river estuary, southern China, Sci. Total Environ., 928, 172321, https://doi.org/10.1016/j.scitotenv.2024.172321, 2024.

Tan, Z., Fuchs, H., Lu, K., Hofzumahaus, A., Bohn, B., Broch, S., Dong, H., Gomm, S., Häseler, R., He, L., Holland, F., Li, X., Liu, Y., Lu, S., Rohrer, F., Shao, M., Wang, B., Wang, M., Wu, Y., Zeng, L., Zhang, Y., Wahner, A., and Zhang, Y.: Radical chemistry at a rural site (Wangdu) in the North China Plain: observation and model calculations of OH, HO_2 and RO_2 radicals, Atmos. Chem. Phys., 17, 663–690, https://doi.org/10.5194/acp-17-663-2017, 2017.

Tan, Z., Lu, K., Dong, H., Hu, M., Li, X., Liu, Y., Lu, S., Shao, M., Su, R., Wang, H., Wu, Y., Wahner, A., and Zhang, Y.: Explicit diagnosis of the local ozone production rate and the ozone-NO_x-VOC sensitivities, Sci. Bull., 63, 1067–1076, https://doi.org/10.1016/j.scib.2018.07.001, 2018a.

Tan, Z., Rohrer, F., Lu, K., Ma, X., Bohn, B., Broch, S., Dong, H., Fuchs, H., Gkatzelis, G. I., Hofzumahaus, A., Holland, F., Li, X., Liu, Y., Liu, Y., Novelli, A., Shao, M., Wang, H., Wu, Y., Zeng, L., Hu, M., Kiendler-Scharr, A., Wahner, A., and Zhang, Y.: Wintertime photochemistry in Beijing: observations of RO_x radical concentrations in the North China Plain during the BEST-ONE campaign, Atmos. Chem. Phys., 18, 12391–12411, https://doi.org/10.5194/acp-18-12391-2018, 2018b.

Tan, Z., Lu, K., Hofzumahaus, A., Fuchs, H., Bohn, B., Holland, F., Liu, Y., Rohrer, F., Shao, M., Sun, K., Wu, Y., Zeng, L., Zhang, Y., Zou, Q., Kiendler-Scharr, A., Wahner, A., and Zhang, Y.: Experimental budgets of OH, HO_2, and RO_2 radicals and implications for ozone formation in the Pearl River Delta in China 2014, Atmos. Chem. Phys., 19, 7129–7150, https://doi.org/10.5194/acp-19-7129-2019, 2019.

Tan, Z., Ma, X., Lu, K., Jiang, M., Zou, Q., Wang, H., Zeng, L., and Zhang, Y.: Direct evidence of local photochemical production driven ozone episode in beijing: a case study, Sci. Total Environ., 800, 148868, https://doi.org/10.1016/j.scitotenv.2021.148868, 2021.

Tang, R., Zheng, Z., and Chen, X.: Measurement report: development of a portable peroxy radical measurement system, Zenodo, https://doi.org/10.5281/zenodo.18346203, 2026.

Thornton, J. A., Wooldridge, P. J., Cohen, R. C., Martinez, M., Harder, H., Brune, W. H., Williams, E. J., Roberts, J. M., Fehsenfeld, F. C., Hall, S. R., Shetter, R. E., Wert, B. P., and Fried, A.: Ozone production rates as a function of NO_x abundances and HO_x production rates in the nashville urban plume, J. Geophys. Res.-Atmos., 107, https://doi.org/10.1029/2001JD000932, 2002.

Wang, H., Liu, Y., Chen, X., Gao, Y., Qiu, W., Jing, S., Wang, Q., Lou, S., Edwards, P. M., Huang, C., and Lu, K.: Unexpected fast radical production emerges in cool seasons: implications for ozone pollution control, Natl. Sci. Open, 1, 20220013, https://doi.org/10.1360/nso/20220013, 2022.

Wang, H., Wang, H., Lu, X., Lu, K., Zhang, L., Tham, Y. J., Shi, Z., Aikin, K., Fan, S., Brown, S. S., and Zhang, Y.: Increased night-time oxidation over China despite widespread decrease across the globe, Nat. Geosci., 16, 217–223, https://doi.org/10.1038/s41561-022-01122-x, 2023a.

Wang, J., Zhang, Y., Zhao, W., Wu, Z., Luo, S., Zhang, H., Zhou, H., Song, W., Zhang, W., and Wang, X.: Observationally constrained modeling of peroxy radical during an ozone episode in the pearl river delta region, china, J. Geophys. Res.-Atmos., 128, e2022JD038279, https://doi.org/10.1029/2022JD038279, 2023b.

Wang, J., Zhang, Y., Xiao, S., Wu, Z., and Wang, X.: Ozone formation at a suburban site in the pearl river delta region, china: role of biogenic volatile organic compounds, Atmosphere-Basel, 14, 609–625, https://doi.org/10.3390/atmos14040609, 2023c.

Wei, N., Zhao, W., Yao, Y., Wang, H., Liu, Z., Xu, X., Rahman, M., Zhang, C., Fittschen, C., and Zhang, W.: Peroxy radical chemistry during ozone photochemical pollution season at a suburban site in the boundary of jiangsu–anhui–shandong–henan region, china, Sci. Total Environ., 904, 166355, https://doi.org/10.1016/j.scitotenv.2023.166355, 2023.

Whalley, L. K., Blitz, M. A., Desservettaz, M., Seakins, P. W., and Heard, D. E.: Reporting the sensitivity of laser-induced fluorescence instruments used for HO_2 detection to an interference from RO_2 radicals and introducing a novel approach that enables HO_2 and certain RO_2 types to be selectively measured, Atmos. Meas. Tech., 6, 3425–3440, https://doi.org/10.5194/amt-6-3425-2013, 2013.

Wolfe, G. M., Marvin, M. R., Roberts, S. J., Travis, K. R., and Liao, J.: The Framework for 0-D Atmospheric Modeling (F0AM) v3.1, Geosci. Model Dev., 9, 3309–3319, https://doi.org/10.5194/gmd-9-3309-2016, 2016.

Wood, E. C. and Charest, J. R.: Chemical amplification – cavity attenuated phase shift spectroscopy measurements of at-

mospheric peroxy radicals, Anal. Chem., 86, 10266–10273, https://doi.org/10.1021/ac502451m, 2014.

Wood, E. C., Deming, B. L., and Kundu, S.: Ethane-based chemical amplification measurement technique for atmospheric peroxy radicals, Environ. Sci. Tech. Let., 4, 15–19, https://doi.org/10.1021/acs.estlett.6b00438, 2017.

Yang, C., Zhao, W., Fang, B., Yu, H., Xu, X., Zhang, Y., Gai, Y., Zhang, W., Chen, W., and Fittschen, C.: Improved chemical amplification instrument by using a nafion dryer as an amplification reactor for quantifying atmospheric peroxy radicals under ambient conditions, Anal. Chem., 91, 776–779, https://doi.org/10.1021/acs.analchem.8b04907, 2019.

Yang, X., Lu, K., Ma, X., Gao, Y., Tan, Z., Wang, H., Chen, X., Li, X., Huang, X., He, L., Tang, M., Zhu, B., Chen, S., Dong, H., Zeng, L., and Zhang, Y.: Radical chemistry in the Pearl River Delta: observations and modeling of OH and HO_2 radicals in Shenzhen in 2018, Atmos. Chem. Phys., 22, 12525–12542, https://doi.org/10.5194/acp-22-12525-2022, 2022.

Yu, H., Wei, N. N., Xu, X. Z., Liu, Q. Q., Yao, Y. C., Zhao, W. X., and Zhang, W. J.: Characteristics of Summer O3 Formation in the Western Suburbs of Hefei Based on Total Peroxy Radical Observations, Environm. Sci., 44, 1974–1984, https://doi.org/10.13227/j.hjkx.202206116, 2023 (in Chinese).

Zhang, G., Hu, R., Xie, P., Hu, C., Liu, X., Zhong, L., Cai, H., Zhu, B., Xia, S., Huang, X., Li, X., and Liu, W.: Intensive photochemical oxidation in the marine atmosphere: evidence from direct radical measurements, Atmos. Chem. Phys., 24, 1825–1839, https://doi.org/10.5194/acp-24-1825-2024, 2024.

Zheng, Z., Wang, H., Chen, X., Wang, J., Li, X., Lu, K., Yu, G.-H., Huang, X., and Fan, S.: A mini broadband cavity enhanced absorption spectrometer for nitrogen dioxide measurement on the unmanned aerial vehicle platform, Atmos. Environ., 321, 120361, https://doi.org/10.1016/j.atmosenv.2024.120361, 2024.

Zou, Z., Chen, T., Chen, Q., Sun, W., Han, S., Ren, Z., Li, X., Song, W., Ge, A., Wang, Q., Tian, X., Pei, C., Wang, X., Zhang, Y., and Wang, T.: Observation and modeling of atmospheric OH and HO_2^* radicals at a subtropical rural site and implications for secondary pollutants, Atmos. Chem. Phys., 25, 8147–8161, https://doi.org/10.5194/acp-25-8147-2025, 2025.